

High Thermoelectric Performance in Sn-Substituted α -As₂Te₃

J. B. Vaney¹, J. Carreaud², G. Delaizir², A. Piarristeguy³, A. Pradel³, E. Alleno⁴, J. Monnier⁴,
E. B. Lopes⁵, A. P. Gonçalves⁵, A. Dauscher¹, C. Candolfi¹, B. Lenoir^{1*}

¹*Institut Jean Lamour (IJL), UMR 7198 CNRS-Université de Lorraine, Nancy, France*

²*Science des Procédés Céramiques et de Traitements de Surface (SPCTS), UMR CNRS 7315-
Université de Limoges, Limoges, France*

³*Institut Charles Gerhardt (ICG), UMR 5253 CNRS-Université de Montpellier, France*

⁴*Institut de Chimie et des Matériaux Paris Est (ICMPE), UMR 7182 CNRS-Université Paris-
Est Créteil, Thiais, France*

⁵*C2TN, Instituto Superior Técnico, Universidade de Lisboa, Lisboa, Portugal*

Abstract

Lead chalcogenides PbX (X = Te, Se, S) have been the materials of choice for thermoelectric power generation at mid-range temperatures (500 – 700 K). Here, we report on a new family of chalcogenides α -As₂Te₃ that exhibits similar thermoelectric performances near 500 K. Sn doping in *p*-type polycrystalline α -As_{2-x}Sn_xTe₃ ($x \leq 0.075$) provides an efficient control parameter to tune the carrier concentration leading to thermopower values that exceed 300 $\mu\text{V K}^{-1}$ at 500 K. Combined with the structural complexity of the monoclinic lattice that results in extremely low thermal conductivity (0.55 $\text{W m}^{-1} \text{K}^{-1}$ at 523 K), a peak *ZT* value of 0.8 is achieved at 523 K for $x = 0.05$. A single-parabolic band model is found to capture well the variations in the transport properties with the Sn concentration and suggests that higher *ZT* values could be achieved through band structure engineering. These results

surpass those obtained in the sister compounds $\beta\text{-As}_{2-x}\text{Sn}_x\text{Te}_3$ and further show that $\alpha\text{-As}_2\text{Te}_3$ based materials are competitive with other chalcogenides for thermoelectric applications at intermediate temperatures.

Electronic Supplementary Information (ESI) available: Rietveld refinements of the PXRD patterns of the $\alpha\text{-As}_{2-x}\text{Sn}_x\text{Te}_3$ samples; BSE images and X-ray mapping; DSC traces; Electrical resistivity data plotted as $\ln \rho$ versus T^{-1} ; High-temperature transport properties of a second specimen of $\alpha\text{-As}_2\text{Te}_3$; Pisarenko plot; Temperature dependence of the specific heat; Crystallographic parameters of the $\alpha\text{-As}_{2-x}\text{Sn}_x\text{Te}_3$ samples.

Corresponding Author

*E-mail: bertrand.lenoir@univ-lorraine.fr

1. Introduction

The thermoelectric potential of a given material is evaluated through its dimensionless figure of merit ZT defined as $ZT = \alpha^2 T / r(k_L + k_e)$.^{1,2} High ZT values are achieved at an absolute temperature T in materials that show an unusual combination of large thermopower α , low electrical resistivity r and low lattice and electronic thermal conductivities k_L and k_e , respectively. Narrow-band-gap semiconductors are usually the best materials that enable achieving a fine balance between these conflicting requirements.^{1,2} In particular, several families of semiconductors investigated over the last years crystallize in a complex unit cell that leads to extremely low lattice thermal conductivity. High ZT values then emerge when the electronic properties are properly optimized either through chemical substitutions or by filling the voids in open-framework structures. Among others, Zintl phases, Mo-based cluster compounds, clathrates or sulfosalt minerals are prominent examples of materials in which such a combination of transport properties was demonstrated.³⁻²⁰

All these families share the common characteristic of exhibiting their maximum ZT at high temperatures, typically between 700 and 1000 K. Near room temperature, however, the state-of-the-art solid solutions $(\text{Bi,Sb})_2(\text{Se,Te})_3$ still represent the best known thermoelectric materials to date.^{1,2} The As-based analogue $\beta\text{-As}_2\text{Te}_3$ represents another member of this family that was recently proposed to harbor topologically-protected surface states when a uniaxial strain is applied along the c axis of the rhombohedral crystal structure (Figure 1).²¹ The β nomenclature refers to the fact that this binary compound also crystallizes with a monoclinic unit cell referred to as the α form.²²⁻²⁵ The crystal structure of $\alpha\text{-As}_2\text{Te}_3$, shown in Figure 1, consists of zig-zag chains where As atoms are either trigonally or octahedrally coordinated to the Te atoms yielding two As and three Te sites. Yet, in spite of first-principles

calculations suggesting that ZT values of up to 0.75 at 300 K might be achieved in both compounds,²⁵ their transport properties remain so far largely unexplored.²⁶

In agreement with these calculations, our recent preliminary study of the thermoelectric properties of $\beta\text{-As}_{2-x}\text{Sn}_x\text{Te}_3$ above room temperature revealed a favorable combination of semiconducting-like electronic properties and extremely low thermal conductivity values.²⁷ Substituting Sn for As offered an effective control parameter of the carrier concentration, thereby significantly improving the ZT values up to 0.65 at 423 K for $x = 0.015$. These results motivated us to investigate Sn substitution in its monoclinic derivative $\alpha\text{-As}_2\text{Te}_3$.

Here, we explore the transport properties of polycrystalline $\alpha\text{-As}_{2-x}\text{Sn}_x\text{Te}_3$ ($0.0 \leq x \leq 0.075$) in a wide range of temperatures (2 – 523 K) with the aim of assessing its thermoelectric potential relative to $\beta\text{-As}_2\text{Te}_3$. Our results show that the carrier concentration can be tuned to achieve a maximum ZT of 0.8 at 523 K for $x = 0.05$. Additionally, we used a single parabolic-band model to identify the basic material parameters that govern the transport and from which strategies to achieve higher ZT values may be developed.

2. Experimental Section

2.1 Synthesis

According to the binary As–Te phase diagram, $\alpha\text{-As}_2\text{Te}_3$ decomposes peritectically at 654 K. This low temperature along with the fact that the boiling point of As is below its melting point makes it difficult a direct synthesis using elemental As and Te. Because the β analogue transforms into the α form when annealed above 473 K,²⁸ $\alpha\text{-As}_{2-x}\text{Sn}_x\text{Te}_3$ specimens were synthesized by annealing $\beta\text{-As}_{2-x}\text{Sn}_x\text{Te}_3$ samples at 573 K for 3 days. In a first step, polycrystalline samples of $\beta\text{-As}_{2-x}\text{Sn}_x\text{Te}_3$ with $x = 0.0, 0.025, 0.050$ and 0.075 were

synthesized by direct reaction of stoichiometric amounts of pure elements (As (Goodfellow, 99.99%), Te (5N+, 99.999%) and Sn (Strem Chemicals, 99.999%)) in silica tubes sealed under secondary vacuum. All manipulations were carried out in dry, argon-filled glove boxes. The tubes were subsequently heated in a vertical furnace up to 923 K with a heating rate of 10 K h⁻¹, held at this temperature for 2 hours and eventually quenched in a salt-ice-water mixture. The annealing step was realized by placing directly the quenched ampules in a furnace. The annealed ingots were ground into micron-sized powders before being consolidated by spark plasma sintering (SPS, Dr. Sinter 515S Syntex) at 618 and 573 K (temperatures selected from the sintering window) for the undoped and doped samples, respectively, under 50 MPa of pressure for 2 min. using a graphite die of 10 mm inner diameter. A second sample of α -As₂Te₃ has been prepared in order to probe for possible off-stoichiometry. For this reason, the synthesis conditions were slightly changed. In a first step, β -As₂Te₃ was synthesized by heating the initial mixture of As and Te powders placed in sealed silica tubes up to 1123 K at a rate of 9 K h⁻¹. This temperature was maintained for 2 h before being quenched in a salt-ice-water mixture. The resulting ingot was crushed into micron-sized powders, introduced in another silica tube and annealed at 618 for 3 days to obtain the targeted α -As₂Te₃ phase.

2.2 Structural and Chemical Characterizations

Phase purity and crystallization were verified by powder X-ray diffraction (PXRD) with a Bruker D8 Advance diffractometer (Cu K α 1 radiation) in reflection mode. The lattice parameters were determined by Rietveld analyses of the collected spectra using the Fullprof software. Chemical homogeneity was probed by scanning electron microscopy (SEM) in backscattering electron mode (BSE) and energy dispersive X-ray spectroscopy (EDXS)

elemental mapping using a Quanta 600 FEG (FEI). These experiments were carried out on polished surfaces of bulk pieces of the consolidated samples.

2.3 Electron Probe Microanalysis

Bulk pieces of the densified samples were carefully polished down to 1 μm with alumina powder to obtain appropriate surfaces for analysis. Electron probe microanalysis (EPMA) was performed with a JEOL JXA 8530F equipped with wavelength-dispersive spectrometers. Backscattered electrons were used for imaging the surface of the samples. In order to minimize matrix effects, X-ray intensities of As and Te were compared with those of a calibrated $\beta\text{-As}_2\text{Te}_3$ standard for quantitative analysis. The calibration of this sample was carried out with the isostructural compound Bi_2Te_3 whose deviations from the ideal stoichiometry are below the resolution of the instrument.² Thus, an exact stoichiometry of two Bi atoms and three Te atoms per formula unit was assumed. The chemical compositions of the $\alpha\text{-As}_{2-x}\text{Sn}_x\text{Te}_3$ specimens were determined from analysis of a set of at least 90 different points for each sample.

2.4 Differential scanning calorimetry (DSC)

Differential scanning calorimetry (DSC) measurements were performed on small pieces of the consolidated pellets (~30 mg) loaded into closed-stainless steel crucibles with a DSC121 (Setaram) apparatus. The data were collected under an argon flow from 300 to 673 K. A low heating rate of 2 K min^{-1} was applied in order to ensure a good thermal equilibrium between the sample and the crucible owing to the low thermal conductivity of these compounds in this temperature range.

2.5 Optical absorption

Optical absorption spectra of disk-shaped samples were measured at room temperature by a Thermo Scientific Nicolet 6700 FTIR spectrophotometer equipped with an integrated sphere. The electronic band gaps E_g were determined by applying the Kubelka-Munk theory that relates the measured reflectance R to a value proportional to the absorption coefficient

$$F(R) = (1 - R)^2 / 2R.^{29}$$

2.6 Low-Temperature Transport Properties Measurements

To probe possible anisotropy, the polycrystalline samples were cut both parallel and perpendicular to the pressing direction with a diamond-wire saw. Bar-shaped samples ($\sim 3 \times 2.5 \times 8 \text{ mm}^3$) were used to measure simultaneously the thermopower, electrical resistivity and thermal conductivity between 5 and 300 K using the thermal transport option (TTO) of a physical property measurement system (PPMS, Quantum Design). These measurements were carried out by brazing four copper leads onto the surface of the samples with a low melting point braze. The same samples were used to determine the Hall resistivity r_H from measurements of the transverse electrical resistivity r_{xy} with the AC transport option of a PPMS. To this end, a five-wire configuration was utilized by soldering five copper wires onto the samples using the same braze as for the TTO measurements. r_{xy} was measured under magnetic fields m_0H ranging between -1 and +1 T. The data were corrected for slight misalignment of the contacts by applying the formula $r_H = \frac{r_{xy}(m_0H) - r_{xy}(-m_0H)}{2}$. The Hall coefficient R_H was determined from the slope of the $r_H(m_0H)$ data in the limit

$m_0 H \rightarrow 0$. Note that for some samples ($x = 0.0$ and $x = 0.025$), the high electrical resistivity measured below 100 K did not allow using a five-wire configuration.

We stress here that the anisotropic crystal structure described in the $C2/m$ space group leads to a galvanomagnetic tensor with a maximum of five independent Hall coefficients.³⁰ Hence, the R_H values will depend on the orientation of the sample, making it challenging to analyze in detail the galvanomagnetic properties. Although the anisotropy as seen by PXRD and transport properties measurements remains moderate (except for the high-temperature thermopower of the binary compound), the R_H values measured show some anisotropy. The difference between the values measured parallel and perpendicular to the pressing direction evolves with the Sn content from 6% for $x = 0.0$ and 0.025 up to 15% in the $x = 0.075$ sample. Keeping this in mind, we shall use the Hall carrier concentration (p) and Hall mobility (m_H) values inferred in the parallel direction within a single-band approximation ($p = 1/R_H e$ with e the elementary charge $m_H = R_H / r$) to analyze the transport as a first approximation. Note that using the values obtained in the perpendicular direction would neither change the analysis nor our general conclusions.

Specific heat measurements were carried out between 2 and 300 K on a small bulk piece of the $x = 0.0$ sample (~20 mg) using the dedicated option of the PPMS. Apiezon N grease was used to ensure a good thermal coupling between the sample and the platform of the sample holder.

Ultrasonic measurements were performed at 300 K to obtain the longitudinal and transverse sound velocities. Honey was used to improve the contact between the piezoelectric transducers and the samples (~ 0.5 mm in thickness).

2.7 High-Temperature Transport Properties Measurements

Another set of bar-shaped samples (typical dimensions $\sim 1 \times 1 \times 8 \text{ mm}^3$) were also cut in the two directions to probe the electrical resistivity and the thermopower between 300 and 523 K. These two measurements were carried out simultaneously with a ZEM-3 apparatus (Ulvac-Riko). Thermal conductivity was determined from 300 up to 523 K via thermal diffusivity measurements performed under argon flow on disk-shaped samples ($\sim 10 \text{ mm}$ in diameter) for the parallel direction and on prism-shaped ($\sim 6 \times 6 \times 1 \text{ mm}^3$) for the perpendicular direction using a LFA 427 (Netzsch) equipment. Prior to these measurements, the samples were spray-coated with a thin layer of graphite to ensure a homogeneous signal absorption and emission on the respective surfaces. The thermal diffusivity a is related to the thermal conductivity by the relation $k = aC_p\rho_V$ where C_p is the isobaric specific heat and ρ_V is the density. Specific heat measurements (DSC 403 F3, Netzsch) were performed on the $x = 0.0$ and 0.05 samples in the same temperature range by the continuous scanning method under argon flow. Because of nearly identical values, a linear fit of the high-temperature data of the $x = 0.0$ sample was used for calculating the thermal conductivity of the $\alpha\text{-As}_{2-x}\text{Sn}_x\text{Te}_3$ series. The combined uncertainty in the determination of the ZT values is estimated to $\sim 17\%$ in the temperature range investigated.³¹ The Hall coefficient was also determined on samples cut in both directions with a home-made apparatus using the van der Pauw configuration. These measurements were performed between 300 and 420 K under dynamic vacuum on thin square samples ($\sim 1 \times 6 \times 6 \text{ mm}^3$) under applied magnetic fields ranging between -1 and $+1\text{T}$.

3. Results and discussion

3.1 Phase purity, chemical homogeneity and thermal behavior

All the polycrystalline samples show experimental densities higher than 98% of the theoretical densities. Unlike the β -As_{2-x}Sn_xTe₃ compounds for which a preferred orientation was noticeable, the PXRD data did not reveal any significant degree of anisotropy. The PXRD patterns, shown in Figure S1 to S4 (Electronic Supplementary Information), demonstrate that the monoclinic phase was obtained as the main phase in all samples. In addition to the reflections of α -As₂Te₃ that were indexed with the monoclinic space group *C2/m*, weak additional peaks are present for some compositions that can be attributed to the cubic AsTe compound and elemental Te. Attempts at synthesizing samples with a higher Sn content ($x = 0.1$) led to an increased amount of secondary phases suggesting that the solubility limit of Sn in α -As₂Te₃ is close to 0.075. SEM images collected in backscattering electron mode (Figure S5 in Electronic Supplementary Information) further corroborated the presence of minute amounts of elemental Te. Elemental mapping images taken on the Sn-doped samples indicate that Sn is homogeneously distributed. This conclusion is further corroborated by the EPMA results that did not reveal any Sn-containing impurities regardless of the nominal composition. Average compositions from EPMA are listed in Table 1. An excellent agreement between the nominal and actual compositions is observed for all samples. The lattice parameters, derived from Rietveld refinements against the PXRD data and summarized in Table S1 (Electronic Supplementary Information), indicate that the unit cell volume expands in a nearly linear manner up to $x = 0.075$ as a result of the larger ionic radius of Sn relative to As. Owing to the presence of two distinct crystallographic As sites, the exact

location of the Sn atoms in the unit cell could not be unequivocally determined from these refinements.

The binary phase α -As₂Te₃ has no melting or decomposition behavior below 600 K as evidenced by the DSC curve shown in Figure S6 (Electronic Supplementary Information). Above this temperature, two well-defined endothermic peaks are observed at 638 and 650 K. Both temperatures agree very well with the reported As-Te binary phase diagram indicating that a mixture of α -As₂Te₃ and Te should evolve with increasing temperature in a two-step process: a first partial melting at 636 K, above which α -As₂Te₃ and liquid coexist, followed by the melting of the binary compound at 654 K. The change of slope in the DSC signal around 612 K might correspond to a third event, although it remains unclear whether this change is intrinsic to α -As₂Te₃.

3.2 Optical Band Gap

Figure 2 presents the absorption spectra against photon energy $h\nu$, where h is the Planck constant and ν is the wave frequency, shown as a Tauc-plot assuming direct transitions for all samples. The signal recorded for the $x = 0.0$ sample shows a steep rise for energies above 0.43 eV. This value is coherent with prior optical absorption measurements (0.46 eV) and with first-principles calculations (0.48 eV) and can thus be attributed to direct transitions across the band gap located along the $\Gamma - Y$ direction according to electronic band structure calculations. The optical spectra of all Sn-doped samples differ from that of the undoped sample since they feature a shallow rise below 0.4 eV followed by a steeper rise around 0.41 – 0.42 eV. The slow rise at low energies might be either due to impurity states in the band gap or intraband transitions while the second increase in absorption may be attributed to interband transitions across the band gap. This interpretation seems further justified by the thermopower

data which feature a broad maximum corresponding to thermal excitations across a band gap of around 0.35 eV in the Sn-substituted samples. These data further show that the optical band gap decreases upon Sn substitution.

3.3 Electronic and galvanomagnetic properties

Figure 3a shows the temperature dependence of the $\rho(T)$ data of the series α -As_{2-x}Sn_xTe₃. Except for the $x = 0.0$ sample below 150 K, no significant difference between measurements parallel and perpendicular to the pressing direction is discernable within the experimental uncertainty, in agreement with the PXRD data. From electronic band structure calculations, α -As₂Te₃ is expected to show a semiconducting behavior. In agreement with this expectation, the electrical resistivity of α -As₂Te₃ is characteristic of lightly-doped semiconductors, with values varying by several orders of magnitude upon cooling to 5 K.²⁶ The substitution of Sn for As does not alter the semiconducting behavior although ρ decreases by one order of magnitude at 300 K on going from $x = 0.0$ to 0.025. Further increasing x then leads to a slight but noticeable increase in ρ above ~ 200 K. At high temperatures, the slow decrease in ρ observed in the $x = 0.050$ and 0.075 samples is likely due to the excitations of minority carriers across the band gap, which decreases with x as revealed by IR absorption spectroscopy.

The low-temperature behavior of $\rho(T)$ can be further understood by considering the electrical transport in non-degenerate semiconductors that can be usually well described by an Arrhenius law $\rho = \rho_0 e^{\frac{D}{T}}$ where $D = E_g / 2k_B$ is the activation energy, E_g is the band gap and k_B is the Boltzmann constant. When the $\rho(T)$ data are plotted as $\ln \rho$ versus T^{-1} , (Figure S7, Electronic Supplementary Information) several distinct regimes can be distinguished. For

all samples, ρ levels off below 40 K in a manner typical of extrinsic conduction mechanisms with $D < 10^{-3}$ meV suggesting that impurity band conduction dominates the electrical transport. The samples enter a different regime of conduction at higher temperatures with activation energies of 0.13 (130 – 520 K), 0.11 (75 – 200 K), 0.045 (80 – 170 K) and 0.040 (80 – 170 K) meV for the $x = 0.0, 0.025, 0.050$ and 0.075 samples, respectively. The temperature range where this regime dominates clearly decreases with increasing x and may be related to charge carriers thermally excited into an impurity band formed by Sn atoms. As we shall see below, Hall effect data provide further experimental evidence in favor of this scenario.

Consistent with the semiconducting nature of these samples, the thermopower steadily increases with temperature in a nonlinear manner in the Sn-substituted specimen (Figure 3b). In contrast, $a(T)$ does not monotonically vary in α -As₂Te₃ but shows a maximum near 250 K, temperature above which a decreases. Above 395 K, a approaches zero in the parallel direction and become negative in the perpendicular direction. Another trait that marks the binary compound as distinct among this series is the anisotropy observed between the parallel and perpendicular directions above ~ 200 K that vanishes upon Sn alloying to within experimental uncertainty. The maximum in $a(T)$, the sign change at high temperatures and the anisotropy are all signatures of mixed conduction that develops in α -As₂Te₃. The anisotropy further suggests that a large asymmetry in the electron-hole density of states effective masses (m^*) exists owing to asymmetry in the dispersion of the valence and conduction bands. A large difference in m^* between electrons and holes seems further supported by the breakdown of the Goldsmid-Sharp relation $E_g \gg 2ea_{\max}T_{\max}$ that relates the energy band gap E_g to the maximum thermopower value a_{\max} reached at the temperature T_{\max} .³² In the present case, this relation would imply a very narrow band gap (75 meV) in

contradiction with the value inferred from absorption measurements (0.43 eV, see Figure 2).

This simple formula is no longer valid either when the material is degenerate or when the

majority-to-minority carrier ratio defined as $A = \frac{m_{maj} \mu_{maj}^* \tau^{3/2}}{m_{min} \mu_{min}^* \tau}$ is very large or very small

(where m is the mobility of the majority and minority carriers).³³ For instance, a similar situation occurs in the Half-Heusler compounds ZrNiSn for which a five-fold difference between the band gaps estimated in n - and p -type samples using the Goldsmid-Sharp relation has been underlined.³⁴

In the Sn-substituted samples, \mathcal{A} ranges between 250 and 300 $\mu\text{V}\cdot\text{K}^{-1}$ at 300 K and rises with temperature before starting to fall near 450 K and 500 K in the $x = 0.050$ and $x = 0.025$ samples, respectively. The maximum reached marks the onset of electron-hole pairs excitation across the energy band gap. The Goldsmid-Sharp relation yields $E_g \sim 0.35$ eV for $x = 0.025$ and 0.30 eV in the $x = 0.050$ and 0.075 samples, in reasonable agreement with the values inferred from absorption spectroscopy. The absence of anisotropy in $\mathcal{A}(T)$ in Sn-substituted specimen further suggests that the closer agreement between the Goldsmid-Sharp relation and the experimental band gaps is mainly due to changes in the above-mentioned A ratio.

The galvanomagnetic properties of the series $\alpha\text{-As}_{2-x}\text{Sn}_x\text{Te}_3$ provide valuable insights into the compositional dependence of r and \mathcal{A} . Hall effect data indicate that all samples exhibit a positive and linear field dependence (not shown) indicative of holes as the dominant carriers, in agreement with the thermopower data. In contrast to $\mathcal{A}(T)$, the Hall data of the binary compound are nearly isotropic with an effective hole concentration p_H of 3.4×10^{18} cm^{-3} at 300 K. We note that due to the strong influence of electrons above 250 K, this value is only an upper limit of the actual hole and electron concentrations in this sample. This carrier density is at least one order of magnitude lower than that calculated (3.125×10^{19} cm^{-3} at 300 K, see Table 2) from electronic band structure calculations in Ref. 25 where no disorder and

$\alpha_{300\text{ K}} = 253.8 \mu\text{V K}^{-1}$ were assumed, indicating that both electrons and holes contribute to the electrical transport. This difference likely originates from electrically-charged native defects due to slight off-stoichiometry, as already observed in the related Bi_2Te_3 -based alloys and suggested in $\beta\text{-As}_2\text{Te}_3$.²⁷ The presence of defects in $\alpha\text{-As}_2\text{Te}_3$ is further corroborated by measurements of the transport properties of a second sample prepared under slightly different synthetic conditions (Figure S8 in Electronic Supplementary Information) for which, *n*-type electrical conduction is observed. The binary $\alpha\text{-As}_2\text{Te}_3$ thus behaves similarly to Bi_2Te_3 where either *p*- or *n*-type conduction can be achieved depending on the synthesis conditions.^{1,2} In Bi_2Te_3 , electrically active charged defects, that is, antisite defects (Bi_{Te} and Te_{Bi}) and vacancies (on the Te or Bi sites), play a central role in determining the carrier concentration and hence, the thermoelectric performances. Antisite defects originate supposedly from the small difference in Pauling electronegativity (PE) between Bi and Te (PE = 2.02 and 2.10, respectively). Because Bi_{Te} (Te_{Bi}) defects and Bi (Te) vacancies act as hole dopants and electron donors, respectively, the type of electrical conduction largely depends on deviations from the ideal stoichiometry.³⁵ Hence, Bi-rich compounds harbor a *p*-type conduction (the main defects are believed to be Te_{Bi}) while Te-rich samples exhibit an *n*-type conduction (the main defects are believed to be Bi_{Te}).³⁶ The similar electronegativity difference between As and Te (PE = 2.18 for As) suggests that antistructure defects equally play a significant role in $\alpha\text{-As}_2\text{Te}_3$. The competition between these two types of defects in samples close to the ideal stoichiometry would naturally explain the presence of holes and electrons in $\alpha\text{-As}_2\text{Te}_3$. This scenario seems consistent with the results obtained on the second sample (Figure S8 in Electronic Supplementary Information) which features similar $r(T)$ but thermopower values as high as $-550 \mu\text{V K}^{-1}$ at 300 K. Slight differences in the subtle balance between the concentration of both types of defects due to different synthetic conditions provide a simple explanation for such stark contrast in $a(T)$.

Upon substituting Sn for As, p_H increases by almost one order of magnitude to $1.35 \times 10^{19} \text{ cm}^{-3}$ for $x = 0.025$ and then smoothly decreases down to $8.1 \times 10^{18} \text{ cm}^{-3}$ for $x = 0.075$. This decrease in the hole concentration naturally explains the increase in both r and \mathcal{A} with x above 300 K. The complex trend observed in $p_H(x)$ suggests a non-rigid-like evolution of the band structure and makes it difficult to draw a definitive conclusion about the donor or acceptor nature of Sn, a situation reminiscent to that observed in $\beta\text{-As}_2\text{Te}_3$.²⁷ This complexity could originate from the amphoteric character of Sn and/or from a change in the intrinsic defect concentration upon substituting Sn for As. The larger difference in electronegativity between As and Sn (PE = 1.96) with respect to As and Te may indeed decrease the antisite defect concentration.

The temperature dependence of the Hall mobility m_H , shown in Figure 4, reveals that above 300 K m_H decreases with temperature in all samples with an approximately $T^{-3/2}$ behavior indicative of acoustic phonon scattering. Below room-temperature, the m_H values increase with increasing x thereby explaining the decrease in r observed below 200 K when x varies from 0.025 to 0.050. Further, m_H sharply decreases before tending to level off below ~ 50 K in the $x = 0.050$ and 0.075 samples. Although this low-temperature decrease suggests that scattering by ionized Sn impurities is also present, m_H rises more steeply than the expected $T^{3/2}$ dependence. In the $x = 0.025$ specimen, the slope approaches T^3 and reduces to T^2 in the other two doped compounds. In this series, grain boundary scattering can be ruled out since the $m_H(T)$ data do not follow the expected relation in any temperature range $m_H(T) \propto T^{-1/2} e^{-\frac{E_B}{k_B T}}$, where E_B is the energy barrier at the grain boundaries. Interestingly, such deviations from the $T^{3/2}$ law were observed in a series of n -type polycrystalline skutterudite $\text{Co}_{1-x}\text{Ni}_x\text{Sb}_3$ ($0 \leq x \leq 0.01$) and in lightly-doped p -type CoSb_3 .³⁷⁻³⁹ These data were recently

reanalyzed and successfully described by a multiband model in the presence of both acoustic phonon and ionized impurity scattering. This model was found to describe remarkably well $m_H(T)$ between 5 and 300 K in both skutterudite systems, providing a consistent interpretation of the nearly constant m_H values at low temperatures and the sharp increase mimicking that of ionized impurity scattering. These analyses demonstrated that an impurity band formed by Ni atoms dominates transport at low temperatures explaining the very low and nearly constant m_H values. Furthermore, the steep increase in m_H was shown to be due to the thermal excitation of carriers from the impurity band to the first valley of the band structure (*i.e.* minimum of the conduction band). The $m_H(T)$ data measured in $\alpha\text{-As}_{2-x}\text{Sn}_x\text{Te}_3$ share strong similarities with those collected in CoSb_3 and $\text{Co}_{1-x}\text{Ni}_x\text{Sb}_3$. In the latter, besides the low-temperature dependence of m_H , increasing the Ni content leads to a shift of the onset of the sharp decrease towards lower temperatures, as tend to do the present m_H data on going from $x = 0.025$ to 0.050 . In addition, impurity band conduction prevailing at low temperatures and extrinsic carrier conduction dominating at moderate temperatures are consistent with the $r(T)$ data. All these clues point to the presence of a Sn impurity band above the valence band maximum at the origin of the anomalous temperature dependence of m_H in $\alpha\text{-As}_{2-x}\text{Sn}_x\text{Te}_3$.

The trend in the a values with the hole concentration has been further analyzed within a single-parabolic-band model (SPB) as a first approximation. This analysis has been performed at 400 K *i.e.* at a temperature where a single carrier type and a well-identified scattering mechanism dominate and below the threshold of the intrinsic regime of conduction. For these reasons, the undoped sample was not included in the present analysis. In the SPB model, the thermopower and hole concentration are expressed as⁴⁰

$$a = \frac{k_B}{e} \frac{(2+r)F_{1+r}(h)}{(1+r)F_r(h)} - \frac{\hbar}{\theta} \quad (1)$$

$$p = 4\rho_C \frac{2m^* k_B T}{h^2} F_{1/2}(h) \quad (2)$$

where k_B is the Boltzmann constant, e is the elementary charge, h is the Planck constant, m^* is the hole density of states effective mass, r is the scattering parameter ($r=0$ for acoustic phonon scattering and $r=2$ for ionized impurities), h is the reduced chemical potential and $F_i(h)$ is the Fermi integral of order i defined as $F_i(h) = \int_0^\infty \frac{z^i dz}{1 + e^{z-h}}$ with z the reduced carrier energy. As shown in Figure S9 (Electronic Supplementary Information), this simple approach describes quite well the $a(p)$ relationship in the hole concentration range covered using a constant m^* value of $1.3 m_e$.

3.4 Thermal transport properties

Figure 5 shows the total thermal conductivity of the α -As_{2-x}Sn_xTe₃ series. The temperature dependence of the specific heat used to calculate the thermal conductivity is shown in Figure S10 (Electronic Supplementary Information). Because of the high electrical resistivity values that lead to negligible electronic contributions, the measured values can be considered to solely reflect the lattice component of the thermal transport. For all samples, $\kappa(T)$ is typical of dielectric crystals with pronounced low-temperature maxima around 25 K. Above this temperature, κ decreases with increasing temperature according roughly to a T^{-1} law. This trend is typical of thermal transport limited by an increasing number of Umklapp scattering events as T increases. The results also evidence a significant degree of anisotropy in α -As₂Te₃ that disappears upon Sn doping. The magnitude of the low-temperature maximum decreases concomitantly with increasing the Sn content, a behavior consistent with enhanced

point-defect scattering, as typically observed in solid solutions. Remarkably, very low thermal conductivity values are achieved at 300 K that further decrease at higher temperatures to reach $\sim 0.55 \text{ W}\cdot\text{m}^{-1}\cdot\text{K}^{-1}$ at 520 K in the $x = 0.050$ and 0.075 samples. These values are nearly identical in $\alpha\text{-As}_{2-x}\text{Sn}_x\text{Te}_3$ and $\beta\text{-As}_{2-x}\text{Sn}_x\text{Te}_3$ and close to those observed in some Se-based chalcogenides.⁴¹⁻⁴⁸

We further compared k_L to the minimum lattice thermal conductivity calculated from the transverse and longitudinal speeds of sound v_T and v_L , respectively, using the model developed by Cahill *et al.*⁴⁹

$$k_m = \frac{\rho}{6\theta} k_B V^{-\frac{2}{3}} \sum_i v_i \frac{\theta_i^2}{\theta} \int_0^{q_i/T} \frac{x^3 e^x}{(e^x - 1)^2} dx \quad (3)$$

In Equation (3), V is the average atomic volume, $\theta_i = v_i(\hbar/k_B)(6\pi^2/V)^{1/3}$ and v_i are the Debye temperature and sound velocity, respectively, of the i th mode. Here, the sum is performed over one longitudinal and two transverse modes. Within this approach, k_m is attained when the phonon mean free path reaches $l = l/2$ which stands for the shortest physically meaningful distance for a phonon of wavelength l . Measurements of the sound velocities carried out on the $x = 0.0$ sample yielded $v_T = 1798 \text{ m s}^{-1}$ and $v_L = 3062 \text{ m s}^{-1}$. Both values are consistent with those determined recently by first-principles calculations.⁵⁰ As shown in Figure 5, k_L approaches k_m ($\sim 0.4 \text{ W m}^{-1} \text{ K}^{-1}$) at high temperatures indicating that the thermal transport is intrinsically optimized in $\alpha\text{-As}_2\text{Te}_3$ with respect to thermoelectric performances.

3.5 Dimensionless thermoelectric figure of merit ZT

The dimensionless figure of merit ZT is shown in Figure 6a as a function of temperature. The combination of intrinsic semiconducting behavior leads to very low ZT values in the undoped sample. Upon substituting Sn for As, the ZT values are significantly improved with a peak value of 0.8 at 523 K in the 0.05 sample. This relatively high value is comparable to those achieved in other thermoelectric chalcogenides such as PbSe or PbS at similar temperatures,⁵¹⁻⁵³ making α -As₂Te₃ an interesting playground to reach high ZT values.

In Figure 6b, the experimental hole concentration dependence of the ZT values is compared to a theoretical curve calculated within the SPB model. The materials properties required in this calculation were obtained using Equations (1) and (2) in addition to the following equations giving the Lorenz number L and the Hall mobility m_H ⁴⁰

$$L = \frac{k_B^2 (1+r)(3+r)F_r(h)F_{2+r}(h) - (2+r)^2 F_{1+r}(h)^2}{e^2 (1+r)^2 F_r(h)^2} \quad (4)$$

$$m_H = \frac{m_0 \sqrt{\rho} F_r(h)}{2G(1+r)F_{1/2}(h)} \quad (5)$$

where m_0 is the intrinsic hole mobility and $G(x)$ is the gamma function. The dependence of ZT on the carrier concentration is then obtained from Equation (6) to (8)

$$ZT = \frac{a^2}{L + (yb)^{-1}} \quad (6)$$

$$b = \frac{m_0 (m^* / m_e)^{3/2} T^{5/2}}{k_L} \quad (7)$$

$$Y = 2eC \frac{\rho k_B m_e}{h^2} \frac{F_r(h)}{G(1+r)} \quad (8)$$

This analysis has also been restricted to 400 K for the same aforementioned reasons. In Equation (7), constant k_L and m_0 values of $0.60 \text{ W m}^{-1} \text{ K}^{-1}$ and $27 \text{ cm}^2 \text{ V}^{-1} \text{ s}^{-1}$, respectively, were used. The experimental hole concentration of $1.3 \times 10^{19} \text{ cm}^{-3}$ is close to the optimum concentration of $4.3 \times 10^{19} \text{ cm}^{-3}$ predicted by the SPB model at 400 K. Yet, this is not to say that further control of the hole concentration may not lead to further optimization of ZT . The limitations of this model are tied to the underlying hypothesis made *i.e.* a constant effective mass and the presence of a single carrier type and single parabolic band. In the present case, the maximum ZT occurs at higher temperatures where the samples experience minority carrier activation. Since this effect is not taken into account in this model, the optimum hole concentration predicted at 400 K is likely underestimated when considering ZT values at higher temperatures. Further, electronic band structure calculations revealed the presence of weakly-dispersive, heavy hole bands located slightly below the Fermi level.^{21,25} Higher hole concentration may allow probing deeper into the valence bands possibly resulting in non-parabolic effects and larger effective masses. These two properties might help maintain high thermopower values despite higher hole concentrations and thus, might contribute to achieve higher ZT values.

4. Conclusion

Our exploration of the transport properties of α -As₂Te₃ revealed that interesting thermoelectric properties may be achieved through a proper control of the carrier concentration. Here, the hole concentration was effectively tuned by Sn alloying leading to a maximum ZT of 0.8 at

523 K for $x = 0.05$. This reasonably high value arises from a favorable combination of high thermopower in a broad temperature range, despite activation of minority carriers, and very low thermal conductivity that approaches the minimum thermal conductivity at high temperatures. The transport properties above 300 K can be fairly well described within a single parabolic band model, which provides guidance for further optimization of α -As₂Te₃. This analysis, combined with the reported electronic band structure of α -As₂Te₃, suggests the possibility to achieve higher ZT values at higher hole concentrations. The similarities between α -As₂Te₃ and the related compounds β -As₂Te₃ and Bi₂Te₃-based alloys further suggest that other elements on both the As and Te sites may help optimize the ZT values making this material competitive with other chalcogenides operating around 500 K.

Conflict of Interest

The authors declare no competing financial interest.

Acknowledgements

The authors would like to thank financial support from the French National Agency (ANR) in the frame of its programme "PROGELEC" (Verre Thermo-Générateur "VTG"). C. C., J.-B. V. and B. L. thank C. Gendarme for the EPMA experiments.

Tables

Table 1. Nominal and actual compositions measured by EPMA on the polycrystalline series α -As_{2-x}Sn_xTe₃. The compositions have been normalized to five atoms per formula unit.

<i>Nominal composition</i>	<i>EPMA</i>
As ₂ Te ₃	As _{1.985} Te _{3.015}
As _{1.975} Sn _{0.025} Te ₃	As _{1.990} Sn _{0.024} Te _{2.986}
As _{1.95} Sn _{0.05} Te ₃	As _{1.929} Sn _{0.047} Te _{3.024}
As _{1.925} Sn _{0.075} Te ₃	As _{1.906} Sn _{0.075} Te _{3.019}

Table 2. Comparison between the experimental and theoretical room-temperature values of the electrical resistivity, thermopower, thermal conductivity and hole concentration of α -As₂Te₃. The experimental data measured in the parallel direction (with respect to the pressing direction) for β -As₂Te₃ are also added. The theoretical data obtained by Boltzmann transport calculations were taken from Ref. 25.

	α -As ₂ Te ₃	α -As ₂ Te ₃ (Boltzmann)	β -As ₂ Te ₃
α ($\mu V K^{-1}$)	137	253.8	110
ρ ($\mu\Omega m$)	4950	35.7	30
κ ($W m^{-1} K^{-1}$)	1.0	0.70	0.50
p (cm^{-3})	3.4×10^{18}	3.125×10^{19}	8.9×10^{19}

Figure Captions

Figure 1. Crystal structure of the β -As₂Te₃ (A) and α -As₂Te₃ (B) phases projected along the b and a axis, respectively. In both pictures, As atoms are red and Te atoms are blue. The primitive unit cell is shown by the black solid lines.

Figure 2. Optical absorption spectra of the series α -As_{2-x}Sn_xTe₃ with $x = 0.0, 0.025, 0.050$ and 0.075 . The intersection of the solid black lines with the x -axis gives an estimation of the optical band gap.

Figure 3. a) Temperature dependence of the electrical resistivity ρ and b) thermopower α as a function of temperature for the α -As_{2-x}Sn_xTe₃ samples with $x = 0.0$ (red circles), 0.025 (blue squares), 0.050 (green triangles) and 0.075 (orange diamonds). In both panels, the filled and open symbols refer to measurements performed parallel and perpendicular to the pressing direction, respectively.

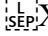
Figure 4. Hall mobility m_H across the α -As_{2-x}Sn_xTe₃ series from Hall effect measurements in the parallel direction for $x = 0.025$ (blue squares), 0.050 (green triangles) and 0.075 (orange diamonds). The solid lines represent the temperature dependence expected for ionized impurities (below 300 K) and acoustic phonons scattering (above 300 K).

Figure 5. Temperature dependence of the total thermal conductivity for α -As_{2-x}Sn_xTe₃ with $x = 0.0$ (red circles), 0.025 (blue squares), 0.050 (green triangles) and 0.075 (orange diamonds) below (panel a) and above (panel b) room temperature. The filled and open symbols refer to measurements performed parallel and perpendicular to the pressing direction, respectively. The horizontal solid black line in panel (b) stands for the minimum thermal conductivity of α -As₂Te₃ calculated using Equation 3.

Figure 6. a) High-temperature dimensionless thermoelectric figure of merit ZT of the α -As_{2-x}Sn_xTe₃ samples for $x = 0.025$ (blue squares), 0.050 (green triangles) and 0.075 (orange diamonds). Owing to the very low values of the $x = 0.0$ sample, only data measured on the Sn-substituted samples are shown. b) Experimental ZT versus hole concentration at 400 K (the symbol scheme used is similar to panel a). The error bars correspond to the estimated experimental uncertainty of 17%. The solid black curve stands for the theoretical hole concentration dependence of ZT calculated within the SPB model.

References

- ¹ H. J. Goldsmid in *Thermoelectric Refrigeration*, Temple Press Books Ltd: London, U.K. **1964**.
- ² *Thermoelectrics and Its Energy Harvesting* (Eds: D. M. Rowe), CRC Press: Boca Raton, FL, **2012**.
- ³ S. R. Brown, S. M. Kauzlarich, F. Gascoin, G. J. Snyder, *Chem. Mater.*, 2006, **18**, 1873-1877.
- ⁴ S. K. Bux, A. Zevalkink, O. Janka, D. Uhl, S. Kauzlarich, G. J. Snyder, J.-P. Fleurial, *J. Mater. Chem. A*, 2014, **2**, 215-220.
- ⁵ E. S. Toberer, A. Zevalkink, N. Crisosto, G. J. Snyder, *Adv. Funct. Mater.*, 2010, **20**, 4375-4380.
- ⁶ T. Yamada, H. Yamane, H. Nagai, *Adv. Mater.*, 2015, **27**, 4708-4713.
- ⁷ U. Aydemir, A. Zevalkink, A. Ormeci, Z. M. Gibbs, S. Bux, G. J. Snyder, *Chem. Mater.*, 2015, **27**, 1622-1630.
- ⁸ T. Zhou, B. Lenoir, M. Colin, A. Dauscher, R. Al Rahal Al Orabi, P. Gougeon, M. Potel, E. Guilmeau, *Appl. Phys. Lett.*, 2011, **98**, 162106.
- ⁹ P. Gougeon, P. Gall, R. Al Rahal Al Orabi, B. Fontaine, R. Gautier, M. Potel, T. Zhou, B. Lenoir, M. Colin, C. Candolfi, A. Dauscher, *Chem. Mater.*, 2012, **24**, 2899-2908.
- ¹⁰ R. Al Rahal Al Orabi, P. Gougeon, P. Gall, B. Fontaine, R. Gautier, M. Colin, C. Candolfi, A. Dauscher, J. Hejtmanek, B. Malaman, B. Lenoir, *Inorg. Chem.*, 2014, **53**, 11699-11709.
- ¹¹ G. S. Nolas, J. L. Cohn, G. A. Slack, S. B. Schujman, *Appl. Phys. Lett.*, 1998, **73**, 178.
- ¹² X. Shi, J. Yang, S. Bai, J. Yang, H. Wang, M. Chi, J. R. Salvador, W. Zhang, L. Chen, W. Wong-Ng, *Adv. Funct. Mater.*, 2010, **20**, 755-763.
- ¹³ B. Du, Y. Saiga, K. Kajisa, T. Takabatake, *Chem. Mater.*, 2015, **27**, 1830-1836.

- ¹⁴ H. Zhang, H. Borrmann, N. Oeschler, C. Candolfi, W. Schnelle, M. Schmidt, U. Burkhardt, M. Baitinger, J.-T. Zhao, Yu. Grin, *Inorg. Chem.*, 2011, **50**, 1250-1257.
- ¹⁵ K. Suekuni, K. Tsuruta, T. Ariga, M. Koyano, *Appl. Phys. Express*, 2012, **5**, 051201.
- ¹⁶ X. Lu, D. T. Morelli, Y. Xia, F. Zhou, V. Ozolins, H. Chi,  X. Zhou, C. Uher, *Adv. Energy Mater.*, 2013, **3**, 342-348.
- ¹⁷ Y. Bouyrie, C. Candolfi, V. Ohorodniichuk, B. Malaman, A. Dauscher, J. Tobola, B. Lenoir, *J. Mater. Chem. C*, 2015, **3**, 10476-10487.
- ¹⁸ X. Lu, D. T. Morelli, Y. Xia, V. Ozolins, *Chem. Mater.*, 2015, **27**, 408-413.
- ¹⁹ P. Qiu, T. Zhang, Y. Qiu, X. Shi, L. Chen, *Energy Environ. Sci.*, 2014, **7**, 4000-4006.
- ²⁰ K. Suekuni, F. S. Kim, H. Nishiate, M. Ohta, H. I. Tanaka, T. Takabatake, *Appl. Phys. Lett.*, 2014, **105**, 132107.
- ²¹ K. Pal, U. V. Waghmare, *Appl. Phys. Lett.*, 2014, **105**, 062105.
- ²² T. C. Harman, B. Paris, S. E. Miller, H. L. Goering, *J. Phys. Chem. Solids*, 1957, **2**, 181-190.
- ²³ N. S. Platakis, *J. Non-Cryst. Solids*, 1977, **24**, 365-376.
- ²⁴ T. J. Scheidemantel, J.F. Meng, J.V. Badding, *J. Phys. Chem. Solids*, 2005, **66**, 1744-1747.
- ²⁵ Y. Sharma, P. Srivastava, *Opt. Mater.*, 2011, **33**, 899-904.
- ²⁶ J.-B. Vaney, J. Carreaud, G. Delaizir, C. Morin, J. Monnier, E. Alleno, A. Piarristeguy, A. Pradel, A. P. Gonçalves, E. B. Lopes, C. Candolfi, A. Dauscher, B. Lenoir, *J. Electron. Mater.*, 2015, DOI: 10.1007/s11664-015-4063-3.
- ²⁷ J.-B. Vaney, J. Carreaud, G. Delaizir, A. Pradel, A. Piarristeguy, C. Morin, E. Alleno, J. Monnier, A. P. Gonçalves, C. Candolfi, A. Dauscher, B. Lenoir, *Adv. Electron. Mater.*, 2015, **1**, 1400008.

- ²⁸ C. Morin, S. Corallini, J. Carreaud, J.B. Vaney, G. Delaizir, J.-C. Crivello, E. B. Lopes, A. Piarristeguy, J. Monnier, C. Candolfi, V. Nassif, G. Cuello, A. Pradel, A. P. Goncalves, B. Lenoir, E. Alleno, *Inorg. Chem.*, 2015, **54**, 9936-9947.
- ²⁹ P. Kubelka, F. Munk, *Z. Tech. Phys.*, 1932, **12**, 593-601.
- ³⁰ Y. C. Akgöz, G. A. Saunders, *J. Phys. C: Solid State Phys.*, 1975, **8**, 1387-1396.
- ³¹ E. Alleno, D. Bérardan, C. Byl, C. Candolfi, R. Daou, R. Decourt, E. Guilmeau, S. Hébert, J. Hejtmanek, B. Lenoir, P. Masschelein, V. Ohorodniichuk, M. Pollet, S. Populoh, D. Ravot, O. Rouleau, M. Soulier, *Rev. Sci. Inst.*, 2015, **86**, 011301.
- ³² H. J. Goldsmid, J. W. Sharp, *J. Electron. Mater.*, 1999, **28**, 869-872.
- ³³ Z. M. Gibbs, H.-S. Kim, H. Wang, G. J. Snyder, *Appl. Phys. Lett.*, 2015, **106**, 022112.
- ³⁴ J. Schmitt, Z. M. Gibbs, G. J. Snyder, C. Felser, *Mater. Horiz.*, 2015, **2**, 68.
- ³⁵ P. Pecheur, G. Toussaint, *J. Phys. Chem. Solids*, 1994, **55**, 327-338.
- ³⁶ J. P. Fleurial, L. Gailliard, R. Triboulet, H. Scherrer, S. Scherrer, *J. Phys. Chem. Solids*, 1988, **49**, 1237.
- ³⁷ Y. Kajikawa, *J. Appl. Phys.*, 2014, **115**, 203716.
- ³⁸ Y. Kajikawa, *J. Appl. Phys.*, 2014, **116**, 153710.
- ³⁹ Y. Kajikawa, *J. Alloys Compd.*, 2015, **621**, 170-178.
- ⁴⁰ V. I. Fistul in *Heavily Doped Semiconductors*, Plenum Press, New York, **1969**.
- ⁴¹ S. Sassi, C. Candolfi, J.-B. Vaney, V. Ohorodniichuk, P. Masschelein, A. Dauscher, B. Lenoir, *Appl. Phys. Lett.*, 2014, **104**, 212105.
- ⁴² Y. He, P. Lu, X. Shi, F. Xu, T. Zhang, G. J. Snyder, C. Uher, L. Chen, *Adv. Mater.*, 2015, **27**, 3639-3644.
- ⁴³ H. Liu, X. Yuan, P. Lu, X. Shi, F. Xu, Y. He, Y. Tang, S. Bai, W. Zhang, L. Chen, Y. Lin, L. Shi, H. Lin, X. Gao, X. Zhang, H. Chi, C. Uher, *Adv. Mater.*, 2013, **25**, 6607-6612.

- ⁴⁴ Q. Tan, L.-D. Zhao, J.-F. Li, C.-F. Wu, T.-R. Wei, Z.-B. Xing, M. G. Kanatzidis, *J. Mater. Chem. A*, 2014, **2**, 17302-17306.
- ⁴⁵ Q. Zhang, E. K. Chere, J. Sun, F. Cao, K. Dahal, S. Chen, G. Chen, Z. Ren, *Adv. Energy Mater.*, 2015, **5**, 1500360.
- ⁴⁶ G. Tan, F. Shi, S. Hao, H. Chi, L.-D. Zhao, C. Uher, C. Wolverton, V. P. Dravid, M. G. Kanatzidis, *J. Am. Chem. Soc.*, 2015, **137**, 5100-5112.
- ⁴⁷ Z.-S. Lin, L. Chen, L.-W. Wang, J.-T. Zhao, L.-M. Wu, *Adv. Mater.*, 2013, **25**, 4800-4806.
- ⁴⁸ J.-S. Rhee, K. H. Lee, S. M. Lee, E. Cho, S. Kim, E. Lee, Y. S. Kwon, J. H. Shim, G. Kotliar, *Nature*, 2009, **459**, 965-968.
- ⁴⁹ D. G. Cahill, S. K. Watson, R. O. Pohl, *Phys. Rev. B*, 1992, **46**, 6131-6140.
- ⁵⁰ H. Deng, *J. Alloys Compd.*, 2015 DOI: 10.1016/j.jallcom.2015.09.195.
- ⁵¹ Y. Pei, Z. M. Gibbs, B. Balke, W. G. Zeier, G. J. Snyder, *Adv. Energy Mater.*, 2014, **4**, 1400486.
- ⁵² Q. Zhang, F. Cao, W. Liu, K. Lukas, B. Yu, S. Chen, C. Opeil, D. Broido, G. Chen, Z. Ren, *J. Am. Chem. Soc.*, 2012, **134**, 10031-10038.
- ⁵³ H. Wang, E. Schechtel, Y. Pei, G. J. Snyder, *Adv. Energy Mater.*, 2013, **3**, 488.